Materials Science & Engineering A 788 (2020) 139532

Contents lists available at ScienceDirect

Materials Science & Engineering A

journal homepage: http://www.elsevier.com/locate/msea

Selective laser melting of austenitic oxide dispersion strengthened steel: Processing, microstructural evolution and strengthening mechanisms

Milad Ghayoor [a,c], Kijoon Lee [a,c], Yujuan He [b], Chih-hung Chang [b], Brian K. Paul [a,c], Somayeh Pasebani [a,c,*]

[a] School of Mechanical, Industrial and Manufacturing Engineering, Oregon State University, Corvallis, OR, 97330, USA
[b] School of Chemical, Biological and Environmental Engineering, Oregon State University, Corvallis, OR, 97330, USA
[c] Advanced Technology and Manufacturing Institute (ATAMI), Corvallis, OR, 97330, USA

ARTICLE INFO

Keywords:
Selective laser melting
Nanocomposite
Oxide dispersion strengthened alloy
304L stainless Steel

ABSTRACT

Oxide dispersion strengthened (ODS) alloys exhibit superior mechanical properties due to the presence of nano-sized thermally stable oxide particles. However, manufacturing of ODS alloys is very complex and composed of numerous time consuming steps such as mechanical alloying, which is one of the main barriers toward the widespread application of ODS alloys. Light mixing of 304L stainless steel powder with sub-micrometer size yttria particles was coupled with selective laser melting (SLM) to produce 304L ODS nanocomposite. The added yttria was dissolved in the matrix due to the high intensity of the laser and altered the rheological properties of the melt and caused balling effect. The SLM 304L ODS alloy presented cellular substructure with a uniform dispersion of yttrium silicate (Y–Si–O) spherical nanoparticles, range 10–80 nm. As a result, the SLM 304L ODS alloy showed a high ultimate tensile strength of ~700 MPa, ductility of ~32% and microhardness of ~350 HV. The underlying mechanism for this strength and ductility improvement are identified. This study provides deep insight into an alternative method of producing ODS alloys with fewer steps and capable of manufacturing complex design geometries.

1. Introduction

Austenitic stainless steels have a desirable creep resistance at high temperature and higher corrosion/oxidation resistance than the ferritic/martensitic stainless steel. However, the tensile properties at higher temperature are limited [1,2]. It is well established that oxide dispersion strengthening (ODS) could improve the tensile properties of a material at high temperatures due to the presence of high density of thermally stable nano-sized oxide particles dispersed within the metal matrix. Essentially, these nanoparticles could impede the dislocations movement and thus improving the creep resistance and tensile properties of the metal matrix at high temperature [3]. The conventional route for preparing austenitic ODS alloy is through mechanical alloying (MA) of the matrix powder and the highly stable nanoparticles, such as Y_2O_3, in a high energy ball milling process. In MA, the Y_2O_3 can be dissociated; forming a supersaturated solution and during the subsequent heat treatment, which includes hot isostatic pressing (HIP), hot rolling, hot extrusion and spark plasma sintering, the ultrafine complex oxides precipitate within the matrix [4–7]. While 304L austenitic ODS alloy demonstrated better mechanical properties, at room and high temperatures, compared to other austenitic ODS alloys [8], there are limited studies on this structural material [9–11]. Morrall et al. [9] investigated the microstructure and tensile properties of MA304L ODS alloy with the addition of 0.7 wt% Zr and followed by a HIP process; indicating the yield stress (YS) of 767 MPa at room temperature, about 531 MPa higher than the 304L manufactured in the identical process. In another work by Zhou et al. [10] on fabricating of the 304 austenitic ODS through the MA and HIP processes, the precipitation of complex Y–Ti–Si–O nanoparticles with spherical shape is reported.

In general, the conventional method of making ODS alloys is very complex and has its own drawbacks such as the numerous steps which make the process, time-consuming and unscalable; inhomogeneous distribution of nanoparticles within the matrix, and induced contamination during MA [11]. These drawbacks hinder the widespread application of ODS alloys despite their promising high temperature performance. Recently, a new sintering process, spark plasma sintering

* Corresponding author. School of Mechanical, Industrial and Manufacturing Engineering, Oregon State University, Corvallis, OR, 97330, USA.
E-mail address: somayeh.pasebani@oregonstate.edu (S. Pasebani).

https://doi.org/10.1016/j.msea.2020.139532
Received 9 January 2020; Received in revised form 3 May 2020; Accepted 4 May 2020
Available online 16 May 2020

(SPS), has been adopted to produce ODS alloy, because it utilizes a pulsed DC current to enhance the sintering rate of compacted powder at relatively lower temperatures with shorter holding time compared to conventional technique [12–14]. However, the SPS is capable to produce simple symmetrical shapes (usually cylindrical designs and disks), and making a part with complex geometry and scaling up the process are not feasible. Furthermore, the heterogeneity of temperature field during the dwell of the temperature cycle could cause the final microstructure to be heterogeneous [15]. Therefore, evaluation and development of other alternative methods to produce ODS alloys is receiving considerable attention among researches with focus on achieving both scalability and consistent properties [16,17].

Selective laser melting (SLM) is a layer-wise powder bed fusion additive manufacturing process [18,19]. The SLM process enables the rapid production of complex geometry component without the time-consuming mold design process or further machining process. In the SLM process, a high energy laser beam selectively scans and melts a thin layer of metal powder bed under a protective atmosphere; consolidating the metal powder. The subsequent solidification of melt could form a layer of the formerly sliced component; using a computer-controlled system. A new layer of metal powder is deposited on the top of the previously solidified layer and the process continues until all the layers of the component are completed [20,21]. The SLM process offers a promising alternative to fabricate components with unique microstructure and mechanical properties [22–26].

In recent years a few studies have utilized mechanically alloyed powders as the feedstock for the SLM process to produce ODS alloy. It is reported [27] that the highest ultimate tensile strength (UTS) for the pre-alloyed ball-milled MA956 powder utilized in a selective laser sintering (SLS) machine was 651 MPa which was 65% of the wrought MA956 steel. This reduction in strength was attributed to the lower density of the manufactured part (97%). According to Boegelein et al. [28] utilizing SLM process to fabricate thin-walled builds, using MA ODS-PM2000 (FeCrAl) powder, as an alternative to HIP process was possible. The YS of as-grown walls (330 MPa) was inferior to the conventionally produced PM2000 alloy (YS = 500 MPa). However, the YS could be improved further (to 450 MPa) by post heat treatment due to presence of atomic Y in the matrix and precipitation of fine Y-enriched particles. Walker et al. [29] demonstrated SLM PM2000 ODS had larger sized yttria-alumina oxides (54–61 nm) and average particle size of 48 nm at a low laser scan speed of 100 mm/s and a high scan speed of 200 mm/s, respectively.

As mentioned before, currently, MA has been utilized as a primary step toward preparing the ODS alloys which is one of the main hurdles in further application of ODS alloys in industry because it is not scalable and is very time-consuming with difference in properties from batch to batch. In this study, a 304L ODS alloy was manufactured using the SLM process without using MA. Rather, the feedstock was prepared by light mixing. Thus, the most time-consuming step in the production of ODS alloys is eliminated. The SLM 304L ODS alloy exhibited very high tensile properties, high microhardness, and improved ductility. The microstructure and mechanical properties of SLM 304L ODS alloy were characterized and correlated. Furthermore, the role of multiple strengthening mechanisms in SLM 304L ODS alloy was discussed.

2. Experimental procedure

2.1. Preparation of feedstock and SLM process

Two starting powder materials were used: gas-atomized 304L stainless steel commercially available from Sandvik, with the chemical composition given in Table 1, and yttrium oxide with the purity of 99.99% from H.C. Starck. The SLM feedstock was prepared by light mixing the 304L powder with 0.5 wt% yttria, in a planetary ball mill (Retsch, PM100). In order to avoid MA; solutionizing of yttria particles into austenitic matrix and severely deforming the metal powder, the rotation speed of 100 rpm and mixing time of 4 h were used. A Malvern Analytical particle analyzer (Mastersizer 3000) was used to evaluate the particle size distribution of powders.

The mixed powder then was used as feedstock to fabricate cylindrical samples with dimensions of D8 × 8 mm and tensile bars using OR Creator SLM machine equipped with a 250 W Yb: YAG fiber laser with a wavelength of 1067 nm and a stainless steel build plate. The oxygen level in the build chamber was kept as low as 100 ppm to minimize oxidation. A preliminary experiment was performed to investigate the process parameters window to obtain components with a relative density of higher than 99%. The obtained optimized SLM parameters were as follows: laser power of 145 W, the scan speed of 100–600 mm/s, the spot size of 50 μm, hatch spacing of 50 μm, and powder layer thickness of 30 μm.

2.2. Microstructure and mechanical characterization

The density of the SLM 304L ODS samples was measured according to the Archimedes method. The Phase identification in the mixed powder and fabricated sample were performed using X-ray diffraction (XRD, Bruker AXS D8 Discover) with Cu K_α target, operated at 40 kV and 40 mA. The metallography specimens were grounded and polished according to the standard procedure and before the examination, were electroetched using a solution of 10 wt% oxalic acid and 90 wt% deionized water, applying 15V DC for 15 s. A FEI Quanta 3D scanning electron microscopy (SEM), coupled with electron dispersive X-ray spectroscopy (EDS) were utilized for a detailed characterization of SLM 304L ODS samples. In addition, electron backscattered diffraction (EBSD) was used to study the texture and grain size of the manufactured specimen. Prior to the EBSD, the sample was polished in a vibratory polisher for 8 h using a 50 nm diamond slurry.

A transmission electron microscope (TEM), model FEI TITAN 80–200 equipped with ChemiSTEM technology, was used to examine the microstructure of SLM 304L ODS samples. The TEM samples were prepared, first by thinning down mechanically to a thickness of about 50–100 μm, and then 3 mm diameter disks were punched out of the samples. These disks were then electropolished using a twin-jet electropolisher (Fischione-110), operated at 15 V and at temperature of −10 °C in an electrolyte solution of 75 vol% methanol and 25 vol% nitric acid. A Leco microhardness tester (M-400A) at a load of 500 g was used to measure the hardness values of SLM 304L ODS samples; the mean of 10 indentations was reported. The tensile test coupon block was built horizontally, with dimensions of 93 × 11 × 9 mm^3 on the build plate, using the parameters which yielded to the highest density. A set of 3 identical dog bones, according to the ASTM E8 was machined using wire electrical discharge machining (EDM) and afterwards the dog bones were polished up to the grit size of 800 before the tensile test. Tensile tests were performed at room temperature on the Instron 5969 machine at a strain rate of 10^{-4} s^{-1} and the head displacement was used to represent the strain.

Table 1
Chemical composition of 304L stainless steel powder.

Element	Cr	Ni	Fe	C	Si	Mn	P	S	N
wt.%	18.853	10.060	Bal	0.017	0.720	1.3	0.012	0.005	0.083

3. Results

3.1. Powder characterization

Fig. 1(a) shows the morphology of 304L and yttria particles. The 304L powder consists of spherical particles with finer satellite attached to the bigger particles with the D_{50} of 33.3 μm. The yttria particles had a prismatic shape with D_{50} of 0.968 μm, as shown in the inset of Fig. 1(a). The morphology of the 304 + 0.5 wt% of yttria after light mixing is shown in Fig. 1(b). The spherical shape of the particles remained unchanged after mixing, and no severe deformation was observed in Fig. 1 (b). The inset in Fig. 1(b) presents the surface of 304 + 0.5 wt% light mixed powder at a higher magnification; suggesting the yttria particles fragmentized to smaller size particles; covering 304L powder particles. Furthermore, the EDS spot analysis on these nanoparticles, as shown in Fig. 1(c), confirmed that these particles are composed of Y and O. The peaks from other elements such as Fe and Cr were collected from the surface of 304L powder due to very small size of nanoparticles.

The D_{50} was measured to be 32.4 μm for mixed 304L+0.5 wt% yttria powder as shown in Fig. 2; shifting the D_{50} toward the smaller particle size and implying that the ball mill process did not severely change the size distribution of 304L powder particles. The particles shape are severely deformed in conventional ball milling process [11], whereas no major effect was observed on the shape, morphology and the initial particle size distribution due to light mixing used in this study. Thus, overall, the shape and morphology of 304L+0.5 wt% yttria powder were qualified for the SLM process.

3.2. XRD results

The X-ray diffraction patterns obtained from the mixed 304 + 0.5 wt % yttria powder and SLM 304L ODS alloy are shown in Fig. 3. After light mixing of 304L and yttria particles, sharp peaks from austenite with FCC structure were detected. However, no peak from yttria was identified likely due to the relatively low amount of yttria (0.5 wt%), causing a low signal to noise ratio to be detected. After SLM process on the mixed 304L+0.5 wt% yttria powder and making 304L ODS alloy, the peak from austenite remained, and no apparent difference in the XRD patterns between the mixed 304L+0.5 wt% yttria powder and the SLM 304L ODS alloy were detected implying that no new phases had been formed, within the detecting limitation of XRD, during the SLM process.

3.3. Density of SLM 304L ODS samples

The relation between relative densities of SLM 304L ODS samples and different volumetric energy density $VED = \frac{P}{vth}$ is shown in Fig. 4, where P is laser power (W), v is scan speed (mm/s), h is hatching space (mm) and t is layer thickness (mm). The relative density increased with increasing VED, reaching to a maximum density of 99% at VED of 387 J/mm^3 and then dropped with further increasing the VED. Hereafter, the VED of 387 J/mm^3 was selected for duplicating samples for the following microstructure and mechanical properties characterization of SLM 304L ODS alloy.

Fig. 5 (a) shows the optical micrograph of cross-section parallel to the build direction of SLM 304L ODS sample after electroetching. The typical hemispherical melt pool boundaries with epitaxial columnar grains (brighter contrast) that grew in the opposite direction of heat flow are shown in Fig. 5 (a). This epitaxial grain growth is dominant in the SLM process due to the combined effect of same crystallographic orientation and identical chemistry of melt and underneath solidified layer providing a condition for heterogeneous nucleation with no barriers [30]. The irregular shape porosities were observed in the cross-section (Fig. 5 (a)). The formation of these porosities is attributed to rapid solidification and lack of fusion due to high viscosity of melt at low VEDs [31]. Fig. 5 (b) shows the optical micrograph of sample with the VED of 387 J/mm^3, no major defect could be seen in the cross-section parallel to the build direction.

Fig. 5 (c) displays a few small particles with bright contrast within the matrix of SLM 304L ODS alloy that were identified as yttrium oxide based on the EDS analysis shown in the inset of Fig. 5 (c). These particles appeared with a high contrast in SEM micrograph because of lower conductivity and charging at the surface of yttria particles. The annotated contour in Fig. 5 (c) shows a balling defect in which a strip-like agglomerated yttria located on the perimeter of a spherical particle. Most of the large agglomerated yttria in the matrix were located on the perimeter of spherical particles, ranged between 40 to 200 μm, as shown in Fig. 5 (c), which implies the major contribution of yttria nanoparticles in formation of balling effect in SLM 304L ODS alloy. According to Ghayoor et al. [32] at VED of ~700 J/mm^3, gas porosities were mainly found in SLM 304L. However, the addition of yttria to the 304L matrix resulted in significant balling effect and consequently reduced the relative density in high VEDs.

3.4. Microstructure of the SLM 304L ODS alloy

The SEM micrograph in Fig. 6 (a) shows a cellular substructure in SLM 304L ODS alloy after electroetching. In general, the high cooling rate of 10^3–10^7 C/s results in a cellular substructure, without formation of any secondary dendrite arms [30]. The SLM 304L ODS alloy contained high number density of spherical nanoparticles within the 304L matrix, shown by arrows in Fig. 6 (a). In a study by Wang et al. [33], forging and hot rolling was used to obtain a uniform distribution of nanoparticles in as-HIPed 304L ODS alloy [33], although in this study, these spherical nanoparticles, approximately 10–80 nm in diameter, uniformly spread throughout the entire sample with a little variation.

The cell size (<500 nm) in SLM 304L ODS alloy was much smaller

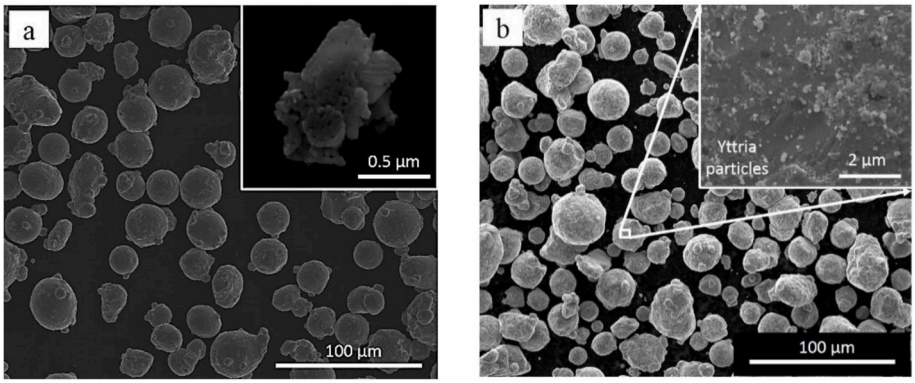

Fig. 1. Morphology of (a) 304L and yttria powder (the inset), (b) the mixed 304 + 0.5 wt% yttria powder, the inset shows the fragmentized yttria nanoparticles covered the surface of a 304L particle and (c) the EDS spot analysis on the fragmentized Y_2O_3 nanoparticles.

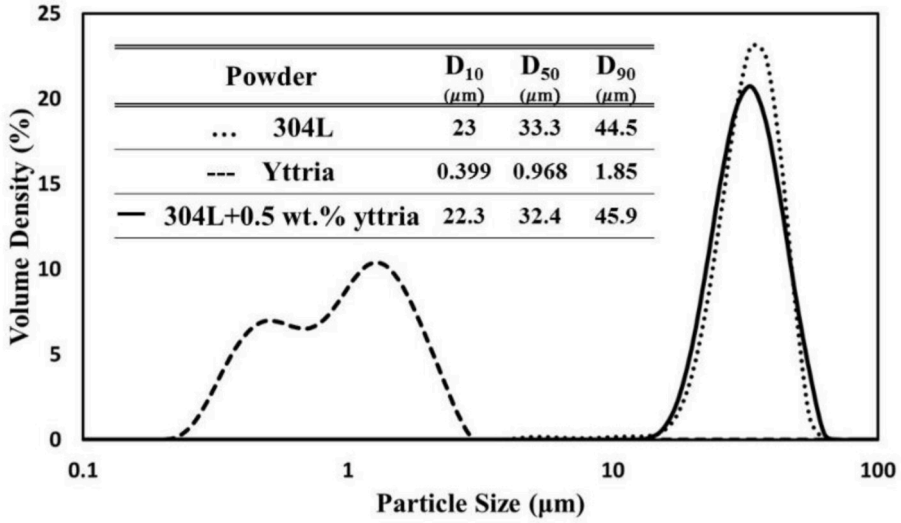

Fig. 2. Particle size distribution histogram of 304L, yttria, and mixed 304L+0.5 wt% yttria powder measured by Malvern particle size analyzer.

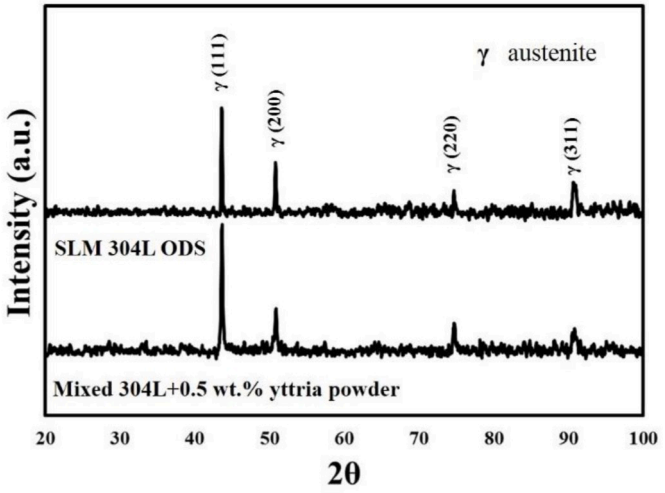

Fig. 3. XRD patterns of mixed 304L+0.5 wt% yttria powder and SLM 304L ODS alloy.

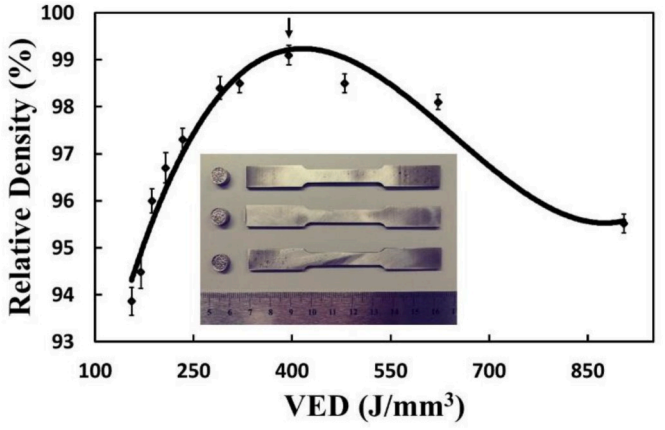

Fig. 4. Relative densities of SLM 304L ODS samples as a function of VED. Inset shows the cylinders (D8 × 8 mm) and tensile bars (gauge l × w × t = 25 × 6 × 2 mm) were built using optimized SLM parameters at VED of 387 J/mm^3 (arrow).

than previously reported cell size of SLM 304L (cell size ~1 μm) [32]. Furthermore, the cellular structure in SLM 304L had a hexagon pattern [32], but the shape of hexagon in SLM 304L ODS alloy was distorted. Both smaller cell size and hexagon shape distortion in SLM 304L ODS alloy could be attributed to the role of added yttria particles. During the solidification stage, the interaction between the nanoparticles and growing cells could split the tip of the cell into the smaller cells [34]. Therefore, multiple interaction with many nanoparticles is predictable for a growing cell which could lead to shape distortion and cells size reduction in SLM 304L ODS alloy compared to SLM 304L.

Microstructure of SLM 304L ODS alloy from cross section perpendicular to build direction is shown in the EBSD inverse pole figure (IPF) map in Fig. 6 (b). The EBSD map revealed columnar grains with a strong texture of (101) [100], as shown in the inset of Fig. 6 (b), pole figures. This strong texture was developed during SLM process due to the directional heat flux and thermal gradient. The grains oriented in the direction of <100> which is the easy growth direction in the cubic systems [32].

The EBSD grains size measurement for the SLM 304L ODS alloy with the VED of 387 J/mm^3 determined the grains size to be 8.1 ± 4.8 μm, which is very similar to the grain size of SLM 304L (average size ~8.2 ± 5.3 μm), previously reported [32]. According to AlMangour [35,36], addition of 15 vol% of TiC nanoparticles to 316L stainless steel could cause microstructural grain refinement and enhance heterogeneous nucleation because of the good wettability of TiC with 316L matrix. Furthermore, in our previous study [37] adding 5 wt% Y_2O_3 to the 304L matrix resulted in a considerable grain refinement. However, EBSD grain size measurement in this study did not show any significant decrease in grain size. It could be due to poor wettability of yttria with stainless steel matrix [38] combined with substantially lower amount of particles, 0.8 vol% (0.5 wt%) here as compared to 15 vol% in AlMangour's studies [35,36] and 8.4 vol% (5 wt%) in our previous study [37].

Fig. 6 (c) presents the grain boundaries misorientation map superimposed on the image quality map; indicating the SLM 304L ODS alloy contained a large fraction of low angle grain boundaries (LAGB, 0–15°, ~76% of the total grain boundaries) associated with subgrains and cellular structures. The kernel average misorientation (KAM), as shown in Fig. 6 (d), calculates the average angular misorientation between a data point and all of its neighbors point. A comparison between Fig. 6 (c) and (d) indicated that the maximum misorientation between neighbors point was concentrated close to the high angle grain boundaries (HAGB); implying higher dislocation densities in HAGB.

The STEM bright field (BF) micrograph of the SLM 304L ODS alloy shown in Fig. 7 (a) revealed the cellular substructure with nanoparticles

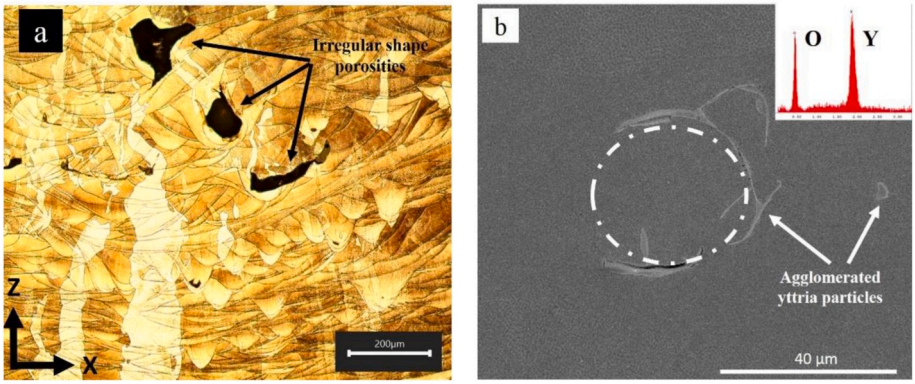

Fig. 5. Optical micrograph obtained from cross section parallel to the build direction of SLM 304L ODS alloy at (a) VED = 242 J/mm^3; presenting irregular shape porosities due to lack of fusion, (b) VED = 387 J/mm^3 with the relative density of 99%, and (c) SEM micrograph showing the balling effect (dashed contour) in SLM 304L ODS alloy manufactured at VED = 645 J/mm^3, the inset shows the EDS results obtained from agglomerated yttria particles in 304L matrix.

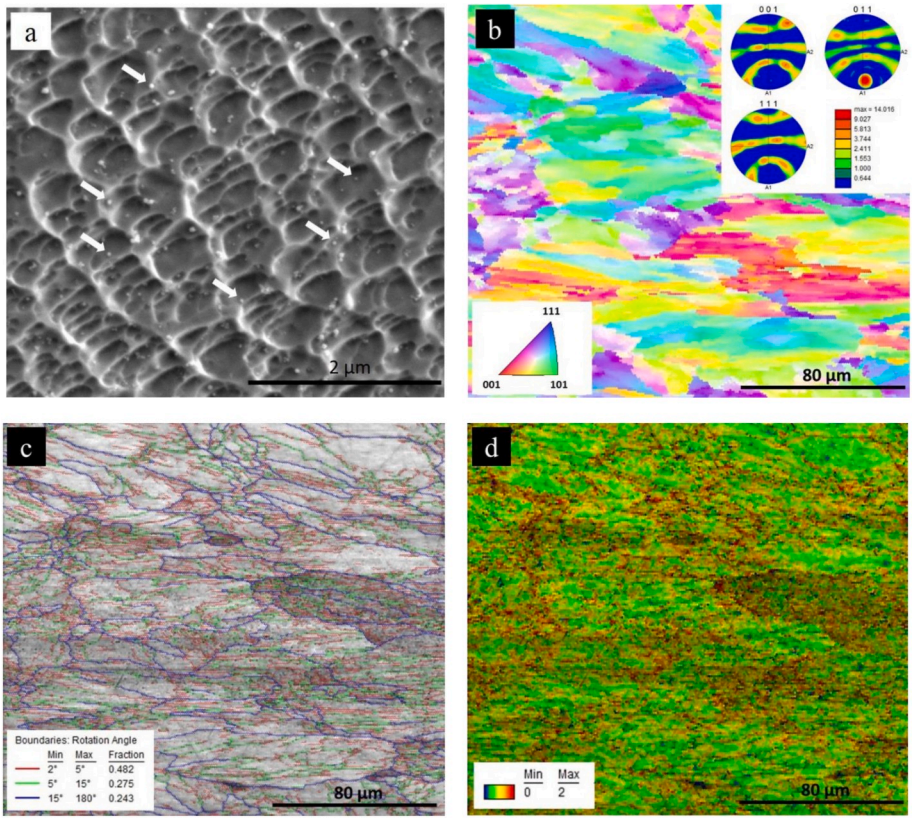

Fig. 6. (a) SEM micrograph of SLM 304L ODS alloy at high magnification showing the cellular substructure and uniform distribution of spherical nanoparticles (shown by arrows) within the 304L matrix, (b) EBSD IPF map and corresponding PF, (c) grain boundary misorientation maps superimposed on image quality maps and (d) kernel average misorientation (KAM) maps, measured in degrees for SLM 304L ODS alloy manufactured at VED = 387 J/mm^3. (For interpretation of the references to color in this figure legend, the reader is referred to the Web version of this article.)

located at cell walls, indicating their role in splitting the growing cell tip at the solidification stage. The underlying mechanism is that the cell tip would be split by the presence of the nanoparticles which would be trapped between the two cell walls. Therefore, the majority of nanoparticles were detected in the cell walls rather than within cells. Cellular walls were decorated with a high density of dislocation, however, the presence of dislocation inside the cells was insignificant. Fig. 7 (b) exhibits a closer look of cells with distorted hexagon patterns caused by nanoparticles. The interaction of dislocations with nanoparticles shown in Fig. 7 (b) determines the role of nanoparticles in impeding dislocation mobility and grain boundary migration and thus improving the mechanical properties of the matrix through dispersion strengthening mechanism [14].

The STEM high angle annular dark-field (HAADF) micrograph and corresponding EDS elemental maps are shown in Fig. 8. The compositional mapping revealed depletion of cell boundaries from Fe, and its enrichment with Cr, Si, and Mn.

Precipitation of spherical nanoparticles, as formerly shown in Fig. 6 (a), are shown with white arrows in HAADF micrograph of Fig. 8. The nanoparticles enriched in yttrium imposed a bright contrast in the STEM micrograph because of high atomic density. Detection of smaller nanoparticles was limited in STEM HAADF micrograph mostly due to the high density of dislocation at cell boundaries inducing extra bright contrast. However, the Y elemental map revealed a uniform distribution of nanoparticles. Table 2 presents the point analysis obtained from Y–Si–O-enriched nanoparticles and matrix. These spherical Y–Si–O nanoparticles were formed likely due to melting of yttria particles during SLM process followed by precipitation during subsequent solidification. Further discussion is provided in section 4.2.

Fig. 8 reveals that the majority of nanoparticles are located within

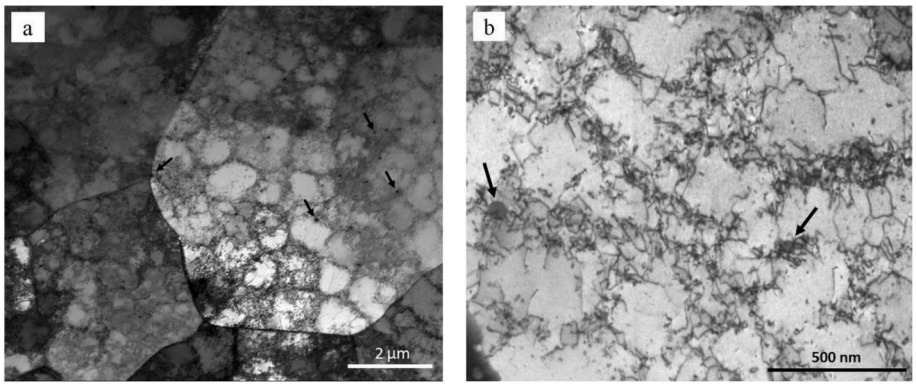

Fig. 7. STEM bright-field (BF) micrograph of SLM 304L ODS alloy (a) the cellular substructure of the as-printed sample with distribution of nanoparticles and (b) distorted hexagon pattern (cell) and a high density of entangled dislocations around nanoparticles. Black arrows point to the nanoparticles in the 304L matrix.

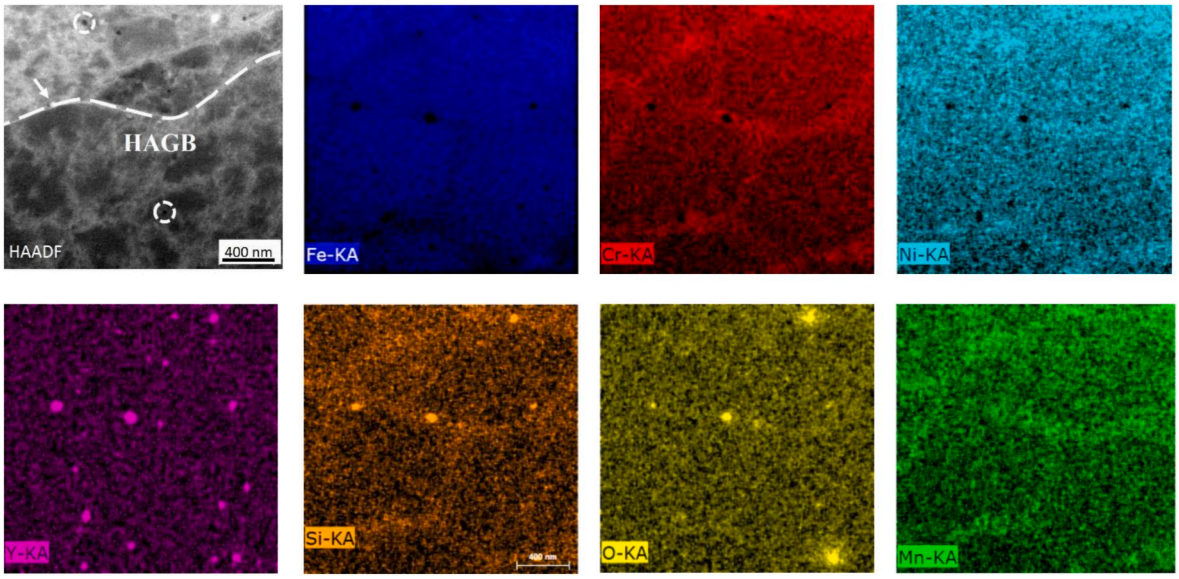

Fig. 8. HAADF (Z-contrast) STEM micrograph of SLM 304L ODS alloy with corresponding EDS elemental maps (arrow points at Y–Si–O-enriched nanoparticle located at HAGB, dashed line shows the HAGB and dashed circles present pores in the matrix).

Table 2
EDS chemical analysis of matrix of SLM 304L ODS alloy and nanoparticles enriched in Y–Si–O (wt.%).

Elements	Fe	Cr	Ni	Mn	Si	Y	O	Total
Matrix (wt.%)	67.45	18.38	10.63	1.05	0.98	0	1.5	100
Nanoparticles (wt.%)	41.27	13.59	6.47	1.59	2.59	12.77	21.73	100

grains rather than grain boundaries which hinders the grain growth at elevated temperature [39,40]. The low wettability of the formed Y–Si–O compound and 304L melt combined with the SLM rapid solidification cause the nanoparticles to be engulfed inside the grains rather than being pushed to the grain boundaries. In addition to the nanoparticles and dislocations, dashed circles in Fig. 8 mark the small-sized pores (~100 nm in size) in the matrix.

3.5. Mechanical properties

The average microhardness value for SLM 304L ODS alloy, with the addition of 0.5 wt% of yttria to 304L matrix, was 350 ± 12 HV, which was about 50% higher compared to the hardness values formerly reported for SLM 304L (235 ± 3 HV) [32]. This increase in hardness is attributed to the homogenous distribution of nanoparticles; enhancing the mechanical properties through dispersion mechanism (Orowan) [14]. The microhardness value in this study was significantly higher than conventionally manufactured austenitic ODS alloys [8]. For example the hardness of rolled and forged austenitic ODS alloy and the hardness of forged, rolled and HIPed austenitic ODS alloy were 245 HV and 280 HV, respectively [41]; in another study on the 316L ODS alloy the microhardness ranged between 275 HV and 306 HV for different condition of ball milling [13], substantially lower than the measured hardness in this study.

The tensile stress-strain curve and the tensile properties of SLM 304L ODS alloy are presented in Fig. 9, illustrating the relatively higher YS and UTS compared to SLM 304L, as reported previously [32] and wrought 304L [42]. The SLM 304L ODS alloy had a YS of 575 ± 8 MPa, UTS of 700 ± 13 and elongation of 32 ± 5% before fracture. Noting that the YS of SLM 304L ODS alloy was about 35 MPa higher than SLM 304L. The mechanical properties of the SLM 304L ODS alloy were compared with our previous work on the SLM 304L and other austenitic ODS alloy

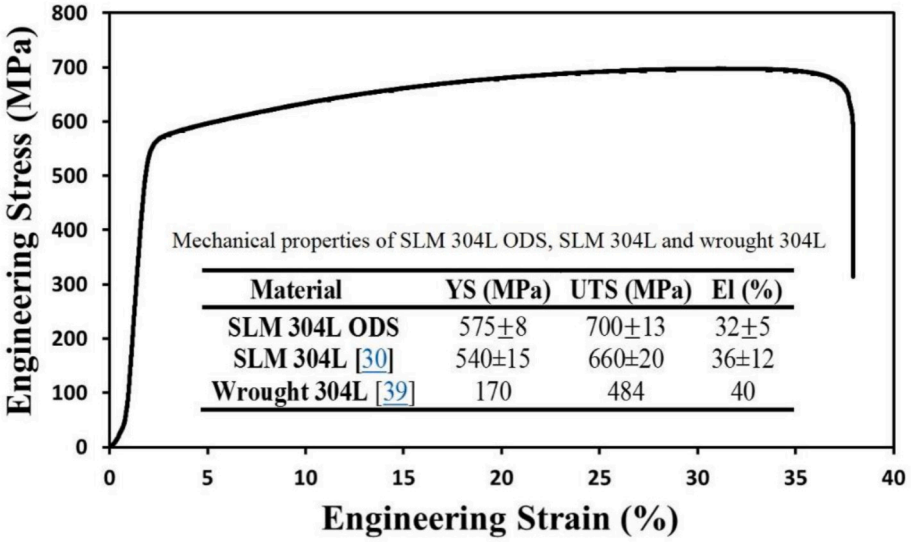

Fig. 9. The tensile stress-strain curve of SLM 304L ODS alloy at room temperature with summary of the mechanical properties of SLM 304L ODS alloy, SLM 304L and wrought 304L listed in the inset table.

prepared using MA process, as shown in Fig. 10. The SLM 304L ODS alloy has a comparable YS and elongation to the most conventionally manufactured austenitic ODS alloys such as HIP 310 ODS, HIP and forged and hot rolled 310 ODS, HIP and hot rolled 316 ODS, HIP 304 ODS, as well as HIP 304L + Zr ODS and previously reported SLM 304L, however, the obtained UTS of SLM 304L ODS alloy was inferior to UTS of referenced studies [9,11,32,33,41,43].

Fig. 11 shows the fracture surface of the SLM 304L ODS alloy. A variety of sub-micrometer to 4 μm dimples were observed across the entire fracture surface as shown in Fig. 11, indicating a ductile fracture behavior. A few small particles were observed in substantially bigger dimples pocket with the maximum diameter of about 1 μm. This observation suggests the large sized particles could act as a potential site for crack initiation and failure of the part.

4. Discussion

4.1. Densification behavior of SLM 304L ODS alloy

Densification behavior of SLM 304L ODS alloy showed a non-linear VED-relative density behavior (Fig. 4), in contrast to the linear behavior of SLM 304L matrix [32]. Irregular shaped porosities containing some unmelted metal powder and agglomerated yttria particles were the major defects in SLM 304L ODS alloy as shown in Fig. 5 (a) and (c) which reduced the relative density of parts.

The physical and chemical properties of powder including morphology, size, laser absorptivity, surface tension, and wettability could affect the SLM process and in particular, densification behavior [44]. Among them, the laser absorptivity of the powder is one of the most influential factors, particularly when two different types of powder with different characteristics are mixed together. It is reported that the addition of non-oxide ceramics such as TiB_2 to 316L SS [45] and

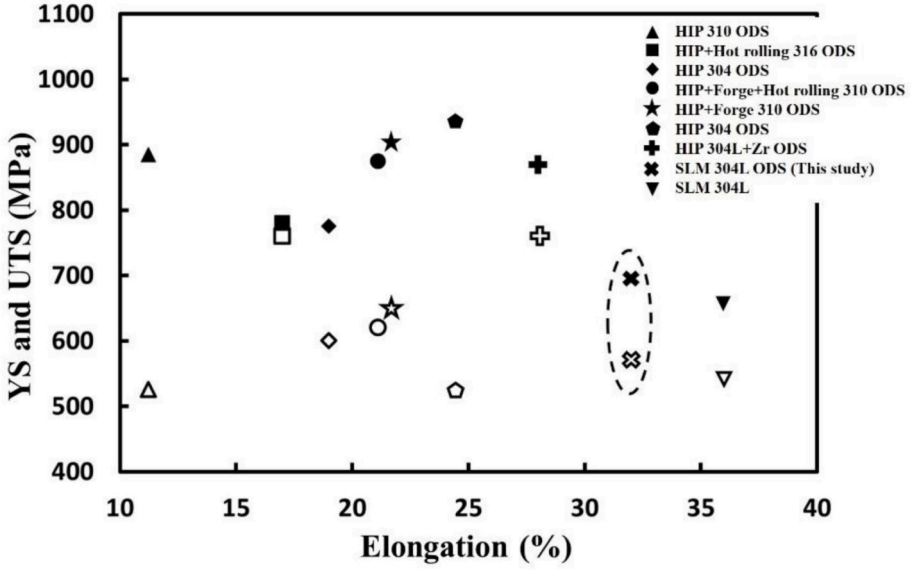

Fig. 10. A comparison between mechanical properties of SLM 304L ODS alloy (the dashed oval) and other conventionally manufactured austenitic ODS alloys and SLM 304L (open markers represent YS and solid markers represent UTS).

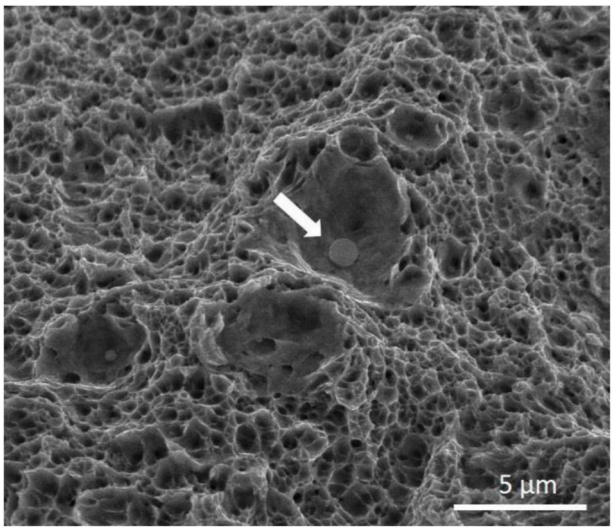

Fig. 11. SEM micrograph showing the fracture surface of SLM 304L ODS alloy and dimples with different sizes (<1–4 µm), the large sized particle at the center of figure (pointed by arrow) could act as a potential site for crack initiation.

nano-TiB_2 to AlSi10Mg [46] enhanced the laser absorptivity of mixed powder and thus improving densification after SLM process. The transmittance constant of yttria for a layer thickness of 55 nm at a wavelength of 1067 nm was about 0.98 [47]. The absorptance was calculated to be < 0.02 (A = 1-0.98 = 0.02) which is negligible compared to the absorptivity constant of stainless steel metal powder at 0.6 [48]. Therefore, the yttria particles could be considered as a transparent material with no significant laser absorptivity enhancement characteristic; suggesting other factors should be considered for the different behavior of SLM 304L ODS alloy compared to SLM 304L.

The dissolution of yttria particles in 304L liquid could decrease the rheological properties of the melt pool. The higher VEDs led to a higher temperature and consequently higher amount of yttria could be dissolved in the melt pool; limiting the flowability of the melt pool. On the other hand, the dynamic viscosity (μ) must be low enough so that the melt can be well-spread on the previously processed powder layer to prevent balling phenomena and other defects. The dynamic viscosity, μ ($kg.m^{-1}.s^{-1}$), of the molten pool can be defined:

$$\mu = \frac{16}{15}\left(\sqrt{\frac{m}{kT}}\gamma\right) \quad (1)$$

where m (kg) is the atomic mass, k ($m^2{\cdot}kg.s^{-2}{\cdot}K^{-1}$) is the Boltzmann constant, T (K) is the absolute temperature, and γ ($kg{\cdot}s^{-2}$) is the liquid surface tension. At higher applied VEDs, the higher temperature would be obtained; leading to lower viscosity, according to Eq. (1). Higher thermal gradient at higher temperature enhanced Marangoni convection providing an unstable condition for the solidification process. Intensified Marangoni convection could lead to accumulation of yttria nanoparticles at the surface of the melt. Furthermore, limited wettability of yttria (the contact angle (θ) on Fe–Cr reported to be 110° [38]) would locally increase the surface tension of melt and cause the melt to spheroidize, known as balling effect. The ball formed Fig. 5 (c) and was covered with a strip-like agglomerated yttria could not get melted due to insufficient laser energy in the subsequent layer and thus would remain as a defect in the matrix and degraded the densification behavior of final part. This phenomenon was also observed in a study on the SLM TiC/Ti bulk composites published by Gu et al. [49].

By decreasing the VED from 967 to 387 J/mm^3, the number of dissolved yttria particles reduced; resulted in a better flowability of the melt on the solidified surface and improved the densification behavior about 3.5%. By further decreasing the VED to 161 J/mm^3, the energy would not be sufficient for providing enough flowability, resulting in lower densification. For lower VEDs (<387 J/mm^3), combined lack of fusion, as shown in Fig. 5 (a), with the unfavorable wetting characteristic of melt promoted irregular shape porosities, as formerly demonstrated by Simchi et al. [50].

Furthermore, unmelted yttria particles would tend toward migrating to the melt pool surface due to buoyancy caused by the substantially lower density of yttria (5.01 gr/cm^3) compared to 304L matrix (8 gr/cm^3). Thus, the unmelted yttria particles could be pushed ahead of the solidification front [51] to join together and form a bigger particle. Forming a bigger particle would intensify the buoyancy force and would cause more balling effect and agglomeration of yttria particles on the surface. Due to low wettability, the agglomerated particles located on top surface could hinder the perfect bonding between the melt and adjacent solidified layer and cause a debonded surface between solidified layers. A detailed characterization on the surface of agglomerated yttria confirmed that these agglomerated yttria particles were sintered together due to the high temperature of melt pool and formed by joining smaller, irregularly shaped yttria particles. Furthermore, the EDS analyses on these large particles confirmed the composition remained as Y_2O_3 as shown in the inset of Fig. 5 (c).

4.2. Formation of the Y–Si–O nanoparticles in SLM 304L ODS alloy

The SLM 304L ODS alloy microstructure consists of uniformly distributed spherical nanoparticles within an alloy matrix as shown in Fig. 6 (a). However, the SEM micrograph of light mixed 304L+0.5 wt% yttria powder (Fig. 1(b)) confirmed that the yttria particles kept their initial irregular shape and the yttria particles did not dissolve into the 304L matrix during the light mixing process. This is in contrast to conventional MA approaches for producing ODS alloys, in which yttrium oxide gets dissociated to atomic Y and O and dissolved in FCC lattice structure of 304L, forming a supersaturated solid solution within the Fe matrix. In conventional MA approach, dissolved yttrium oxide precipitates as nanoclusters during subsequent heat treatment such as hot extrusion or HIP [3]. In this study, the morphology and composition of the nanoparticles were transformed after SLM, suggesting that the yttria particles were melted and dissolved during the SLM process and formed precipitates of Y–Si–O nanoparticles upon solidification from a supersaturated melt solution.

Two different phenomena are proposed for the melting of yttria nanoparticles during the SLM process. Firstly, the 304L powder particles were covered with yttria nanoparticles as shown in Fig. 1(b). So, the distribution of yttria nanoparticles on the surface of metal powder will directly expose them to the incident laser beam as schematically depicted in Fig. 12 (a). In an initial step, the laser energy is absorbed in a narrow layer of any individual 304L powder particles, producing a high temperature on the surface of the particles during the interaction. The high temperature on the surface of powder which could reach to the boiling point of metal powder [52] combined with high surface-to-volume ratio of nanoparticles (size <100 nm) could melt yttria nanoparticles.

Secondly, the yttria nanoparticles that are not exposed to the direct incidence of the laser beam, would be immersed into the melt pool. Alvarez's study [53] on the role of non-stoichiometric in melting process of Y_2O_3 using molecular dynamics simulation showed that the yttria starts to lose its stoichiometry at a temperature of 1500 K, and it could reach to 15% loss of oxygen atoms at high temperatures, as schematically shown in Fig. 12 (b).

According to the phase diagram of Y–O, shown in Fig. 12 (c) [54], losing the oxygen atoms leads to a drop in the melting point of yttria. In other words, the interaction of laser with metal powder initiates the melting process and would elevate the temperature of the melt pool. Simultaneously with increasing the temperature, the more oxygen vacancies would be formed in crystalline structure of yttria, and the O/Y ratio decreases as a result. This decrease in the ratio of O/Y in the crystal

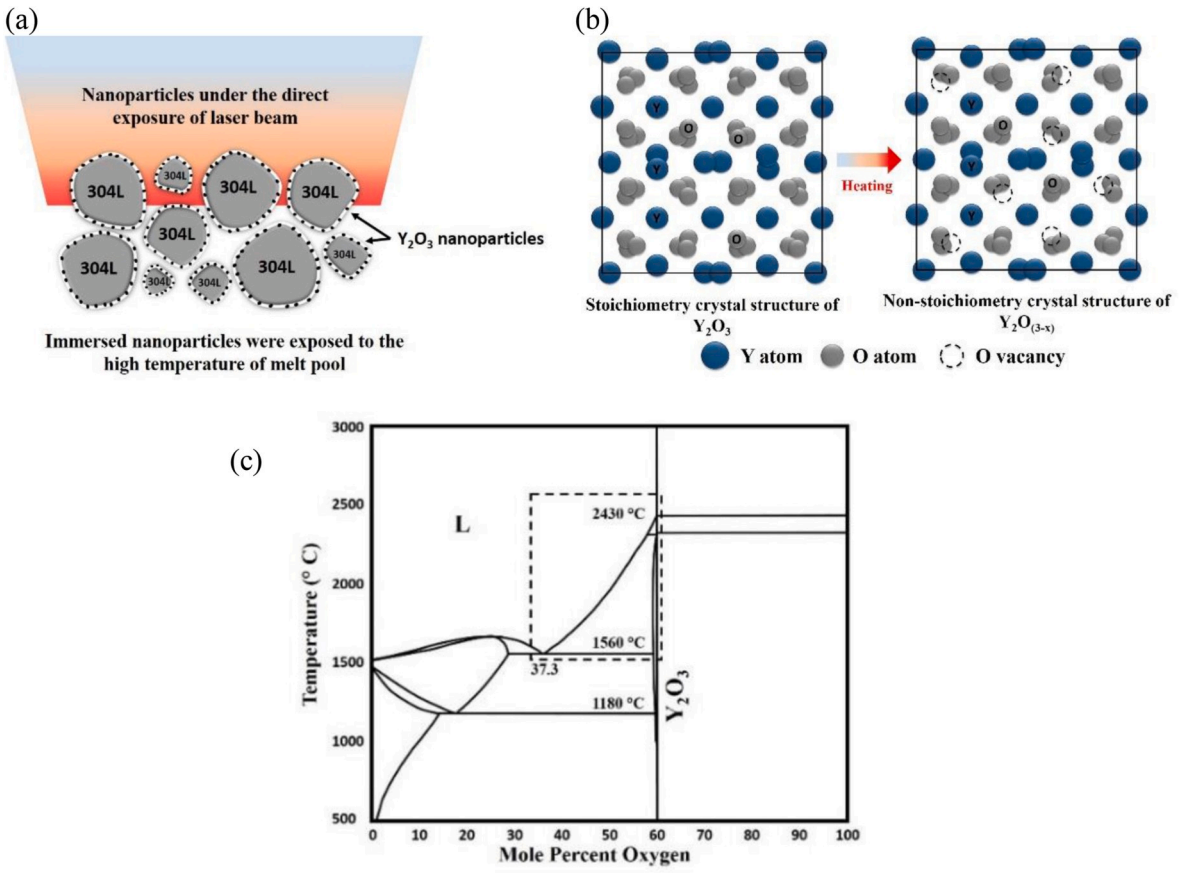

Fig. 12. Schematics showing (a) the prompt interaction of the large diameter of laser beam with the nanoparticles decorating the surface of 304L powder that can be melted due to a high surface to volume ratio associated with nanoparticles (b) the loss of oxygen atoms from crystal structure of stoichiometry-Y_2O_3 upon heating and melting the powder bed resulting in a non-stoichiometric-Y_2O_3, and (c) Y–O phase diagram, presenting loss of oxygen atoms could potentially decrease the melting temperature of Y_2O_3.

structure of yttria could drop the melting point of stoichiometric yttria (2430 °C) potentially down to the maximum predicted temperature (2200 °C) in the melting of austenitic stainless steel during the SLM process [52,55]. Therefore, under the prompt interaction of laser and metal powder, a small fluctuation in the stoichiometric composition of yttria likely dropped the melting point in a thin surface layer of the yttria nanoparticles. This provided an accelerated diffusion path from the core of yttria nanoparticle (stoichiometric-Y_2O_3) to the outer surface of yttria nanoparticle (non-stoichiometric-Y_2O_3) for the oxygen atoms, decreasing the O/Y ratio further and leading to partial or full melting of the yttria nanoparticles. Consequently, the dissolved Y and O atoms would disperse in the melted 304L matrix.

The iron and yttrium are fully immiscible and there is no solid solution formation in Fe–Y phase diagram [56]. According to the EDS analysis on precipitated nanoparticles, as shown in Fig. 8, the precipitated nanoparticles were enriched in yttrium, silicon and oxygen. Therefore, it can be expected, the dissociated yttrium and oxygen atoms would react with the available silicon in the 304L matrix (0.72 wt%) during the subsequent solidification to form yttrium silicate or Y–Si–O-enriched nanoparticles, due to the extreme reactivity of yttrium with silicon and oxygen. The measured binding energy of Y $3d_{5/2}$ in Y–Si–O and Y_2O_3 were 158.2 eV and 156.8 eV, respectively [57]. Furthermore, the binding energy of O 1s in Y–Si–O and Y_2O_3 were 531.8 eV and 529.5 eV, respectively [57], indicating the Y–Si–O required more energy to decompose compared to decomposition of Y_2O_3, and the formation of yttrium silicate was more favorable to the system. The higher energy needed to dissociate the yttrium silicate suggests higher stability of these nanoparticles compared to yttria to impede grain growth and diffusion which is desirable for high temperatures application [3]. It should be noted that, although EDS analysis shows that the majority of nanoparticles were Y–Si–O, in case of the absence of Si atoms, there is a possibility of formation of Y–O compound in SLM 304L ODS alloy. Further investigation will be considered in our future work to identify the exact composition of these nanoparticles.

The nanoparticles were uniformly distributed throughout the matrix as shown in Fig. 6 (a). With diffusion of Y and O atoms in the melt pool and the capillary force which induced Marangoni convection within the melt pool, the solute diffusion was accelerated which facilitated a homogenous distribution of nanoparticles in SLM 304L ODS alloy.

4.3. Mechanical properties of SLM 304L ODS alloy

According to our previous study on SLM 304L [32], the YS was 540 ± 15 MPa and the elongation was 36 ± 12% which were considerably higher than the wrought 304L and these properties were attributed to the fine microstructure and pre-existence of twining formed by rapid cooling and thermal stresses. In this study, the SLM 304L ODS alloy had a YS of 575 ± 8 MPa at room temperature, which was about 6% higher than SLM 304L alloy without the addition of yttria particles. Since the morphology of grains and microstructure in SLM 304L and SLM 304L ODS alloy were very similar, the ~35 MPa increment in YS was likely caused by other strengthening mechanisms. The ~35 MPa increment in YS of SLM 304L ODS alloy compared to SLM 304L could be attributed to different strengthening mechanisms including solid solution strengthening, grain boundary strengthening (Hall-Petch), increase in dislocation density due to the mismatch thermal expansion coefficient and rapid solidification, dispersion of nanoparticles (Orowan) and load-bearing strengthening through strong interfacial bonding between

nanoparticles and the matrix [58].

Because iron and yttrium are essentially immiscible and there is no solid solution in their phase diagram [56], therefore, it can be expected the solid solution strengthening mechanism had no effect on improving the yield strength. Furthermore, due to the infinitesimal amount of nanoparticles (≪0.8 vol%) and smaller size of nanoparticles (10–80 nm) the load-bearing mechanism could be neglected. Thus, the increment in strength ($\Delta\sigma_y$) can be estimated by the following equation:

$$\Delta\sigma_y = \Delta\sigma_{GB} + \Delta\sigma_D + \Delta\sigma_{Oro} \quad (2)$$

where $\Delta\sigma_y$ is the increment in yield strength, $\Delta\sigma_{GB}$ is the grain boundary strengthening contribution, $\Delta\sigma_D$ is the dislocation strengthening contribution, and $\Delta\sigma_{Oro}$ is the Orowan or dispersion strengthening contribution.

The EBSD micrograph of the SLM 304L ODS alloy, showed very fine columnar grains with the average grain size of 8.1 μm (Fig. 6). Therefore, the Hall-Petch relationship could be utilized for estimating the grain boundary strengthening contribution as below:

$$\Delta\sigma_{Hall-Petch} = K\left(d_{ODS}^{-0.5} - d_M^{-0.5}\right) \quad (3)$$

where k is a constant and taken as 0.274 $MNm^{-3/2}$ [59] and d is the grain size. According to our previous study [32], the grain size of the matrix (SLM 304L) was about 8.2 μm. Thus, the calculated strength increment by the grain boundary mechanism ($\Delta\sigma_{GB}$) was ~2.3 MPa.

According to the TEM results shown in Fig. 7, the SLM 304L ODS alloy had a high dislocation density, due to rapid melting and cooling, inducing a high strain to the matrix which intensified the matrix dislocation density. Using different TEM micrographs and adopting the line-intercept method, the average of dislocation density was calculated to be 2.11×10^{14} (m^{-2}) and 2×10^{14} (m^{-2}) for SLM 304L ODS alloy and SLM 304L, respectively. It can be concluded that contribution of dislocations was not found to be significant. In other words, the SLM process itself generated a high density of dislocation in the matrix which may cover the effect of the addition of nanoparticles. Another reason could be the small size and the low amount of added yttria nanoparticles (≪0.8 vol %). In this regard, the increase in strength due to the dislocation density is given by Baily-Hirsch equation [60]:

$$\Delta\sigma_D = \alpha MGb\left(\rho_{ODS}^{0.5} - \rho_M^{0.5}\right) \quad (4)$$

where α is a constant value of 0.25 [61], M is Taylor factor (~3 for fcc polycrystals), G is shear modulus (83 GPa for Fe), b is burger vector (0.25 nm) and ρ is the dislocation density (m^{-2}). The contribution of dislocation strengthening ($\Delta\sigma_D$) was estimated to be ~4 MPa. As such, the contribution of Orowan mechanism to the YS increment in SLM 304L ODS alloy was ~29 MPa. Morell et al. [9] estimated the Orowan strengthening mechanism contribution of Zr-reached nanoparticle in a HIPed and then annealed 304L ODS alloy was 44 MPa, which is similar to our result. The Orowan-Ashby model predicts the contribution of volume fraction of precipitates to YS as below [62]:

$$\Delta\sigma_{Or} = \left(\frac{10.8\sqrt{f}}{D}\right)\ln(1630D) \quad (5)$$

where $\Delta\sigma_{Or}$ represents the precipitation strengthening increment in MPa, f is the precipitate volume fraction (vol%), and D is the mean particle diameter (μm). Here, D was measured to be ~47 nm, and, thus the value of f was estimated as ~0.085 vol% which is significantly lower than the initial yttria particles added to feedstock (0.8 vol%). It can be expected, the remaining amount of the added yttria, which was calculated to be ~90% was mainly agglomerated within the matrix, as formerly shown in Fig. 5 (c), and therefore did not contribute to dispersion strengthening. This analysis shows that in SLM 304L ODS alloy, the dispersion mechanism has a contribution of 5% (~29 MPa) to the YS of 575 MPa. In this regard, other strengthening mechanism; including solid solution, Hall-Petch and increase in dislocation density due to rapid solidification had more significant role compared to dispersion mechanism in strengthening of SLM 304L ODS alloy.

Xu et al. [11] reported UTS of 775 MPa for a 304L ODS alloy which was manufactured by MA and HIP at 1150 °C under a pressure of 200 MPa followed by annealing at 900 °C. The higher UTS in Xu's study [11] compared to our study (UTS = 700 ± 13 MPa) could be attributed to the smaller grain size in their study, reported as 5 μm, through the Hall-Petch mechanism [63]. In another study on the conventional manufacturing of 304 ODS alloy [9], the UTS of 872 MPa was reported for the grain size of 0.42 μm with homogeneously distributed Zr-rich precipitates which was much finer than grain size in our study (8.1 μm). In comparison, the grain size in conventionally manufactured austenitic ODS alloys (0.42–5 μm) due to the adoption of different manufacturing processes, such as hot extrusion or hot rolling, which induce finer grain size, was much smaller than the grain size in our study (8.1 μm) using SLM process; leading to higher tensile properties at room temperature in conventionally manufactured ODS alloys [9–11]. This comparison shows that by reducing the grain size of manufactured part of SLM 304L ODS alloy, there is a potential to achieve higher tensile properties compared to the results obtained in this study. In this regard, Wan et al. [64] demonstrated that by adopting different scan strategies, due to altering the heat flux direction, finer grain size could be achieved, which resulted in improved mechanical properties.

The size of nanoparticles in our study (10–80 nm) were larger than conventionally manufactured ODS alloys which the nanoparticles were in the order of few nm to 20 nm [4,5,9]. In the conventional technique of manufacturing austenitic ODS alloy, it is widely believed that the added yttria particles are dissolved in the matrix during the high energy ball milling. Afterwards, the oxygen-enriched nanoparticles precipitate in subsequent high-temperature consolidation process such as HIP or/and hot extrusion processes [65]. The diffusion of yttrium and other elements with high affinity for oxygen such as Ti and Hf in the matrix play an important role in the kinetics of formation and growth of nanoparticles through the process known as Ostwald ripening mechanism [66,67]. The diffusion coefficient, D_s ($m^2.s^{-1}$), in solid iron follows the Arrhenius equation:

$$D_s = D_0\exp\left(-\frac{E_A}{RT}\right) \quad (6)$$

where D_0 ($m^2.s^{-1}$) is the diffusion coefficient, E_A ($J.mol^{-1}$) is the activation energy for diffusion, T (K) is absolute temperature and R ($J.mol^{-1}.K^{-1}$) is the gas constant. However, the diffusion coefficient in liquid iron, D_l ($m^2.s^{-1}$), would follow the Stokes-Einstein equation:

$$D_l = \frac{kT}{6\,\pi\mu r} \quad (7)$$

where μ ($kg.m^{-1}.s^{-1}$) is dynamic viscosity, k ($m^2{\cdot}kg.s^{-2}.K^{-1}$) is Boltzmann's constant, T (K) is absolute temperature and r (m) is particle radius. As following different mechanism of mass transfer, $D_l \gg D_s$, resulted in faster diffusion of yttrium, silicon, and oxygen in liquid melt pool and enhanced the Ostwald ripening mechanism compared to solid state diffusion. Furthermore, Marangoni convection in the melt pool can facilitate the mass transfer of atoms and thus, larger nanoparticles were formed in SLM 304L ODS alloy compared to the conventional route of manufacturing of ODS alloy in which finer nanoparticles, smaller than 20 nm were precipitated in the matrix [4,5].

In this study, the SLM 304L ODS alloy showed higher ductility and elongation compared to its counterpart using conventional manufacturing techniques, as shown in Fig. 10. The reported elongation for 304 ODS alloy after HIP and annealing heat treatment was 19–28% at room temperature [9,11,33,41]. However, the measured elongation in our study was 32 ± 5% which is slightly higher than conventionally manufactured 304 ODS alloy.

The work hardening is usually generated via accumulation of dislocations; higher dislocations accumulation leads to higher work

hardening, and consequently higher tensile ductility. The ductility of a material can be enhanced mainly through three possible mechanisms; introducing a bimodal microstructure, dispersion of nanoparticles, and increasing work hardening rate [68–70]. The SLM 304L ODS alloy in our study did not show a bimodal microstructure and, presumably, the dispersion of nanoparticle mechanism is involved in both techniques, conventionally manufactured 304 ODS and SLM 304L ODS alloy. The dislocations will be forced to accumulate when they intersect or by-pass the nanoparticles, leading to higher tensile ductility. Thus, the underlying mechanism for this higher elongation could be attributed to the role of higher work hardening rate in SLM 304L ODS alloy. It is well established that nanostructured metallic materials have a very low work hardening rate due to their low dislocation storage efficiency owing to their small grains and/or nearly saturated dislocation density. The dislocations are emitted from and annihilated at grain boundaries without accumulation inside the grains. However, larger grains might have sufficient space within the grains for significant number of dislocations to intersect and tangle with each other and, consequently, accumulate during the deformation [69,71]. In our study, the grain size was 8.1 μm, substantially larger than sub-micrometer grain size reported in conventionally manufactured austenitic 304 ODS alloys that yielded to the elongation of 21% and 28.1% [9,41]. Therefore, the existence of larger grain size in SLM 304L ODS alloy compared to sub-micron grains in conventionally manufactured 304 ODS alloy could be considered as the main mechanism for the elongation improvement in this study. Additionally, due to segregation of alloying elements, Cr and Ni, and a higher density of dislocation in cell boundaries, as shown in Figs. 7 and 8, it can be expected the cell boundaries in SLM 304L ODS alloy could work as potential obstacles for dislocation movement; having the same role as nanoparticles. Interaction of dislocations with cell boundaries should lead to their accumulation within the grains and, therefore, leading to a higher work hardening rate before fracture and higher ductility in SLM 304L ODS alloy, compared to conventionally manufactured counterparts. The aforementioned mechanisms together would be probably the reason for the observed enhanced ductility, however, to unravel the exact underlying mechanism for the higher ductility in this study, more detailed investigation will be carried out in the near future.

5. Conclusions

This study demonstrated that the SLM process can be utilized to produce an ODS alloy in lesser steps compared to conventionally method of manufacturing ODS alloy by eliminating the most time-consuming step, mechanical alloying, which is main hurdle in widespread application of ODS alloys in industry. Furthermore, the intrinsic advantage of additive manufacturing promotes making very complex geometries with ODS alloys using the proposed route in this study. In this study, nearly fully dense austenitic 304L ODS alloy parts were manufactured using optimized parameters in a SLM machine. In order to avoid mechanical alloying, a light mixing approach was employed to prepare the precursor powder of 304L ODS alloy. A detailed investigation was done on the resulting SLM 304L ODS alloy in order to elucidate the effect of added yttria particles on densification behavior, microstructure evolution and mechanical properties of SLM 304L ODS alloy. The main conclusions can be drawn as follows:

1. The highest relative density of 99% was achieved at the VED of 387 J/mm^3. The melted yttria particles altered the rheological properties of SLM 304L ODS alloy; leading to more balling effect. The joined unmelted yttria particles intensified the buoyancy force; resulting in agglomerated yttria particles on the surface of the melt.
2. The SEM and STEM analyses revealed the precipitation of uniformly distributed spherical nanoparticles in the matrix, which EDS analyses showed to be Y–Si–O; being more stable at higher temperature compared to yttria.
3. In addition to the high intensity of the laser beam, the non-stoichiometric composition of yttria at higher temperature likely dropped the melting point of yttria resulting in partial or full melting of the yttria particles in the SLM process and precipitation of Y–Si–O-enriched nanoparticles during solidification.
4. The SLM 304L ODS alloy exhibited a high tensile strength of 700 $\pm$ 13 MPa, improved ductility of 32 $\pm$ 5% and high microhardness of 350 $\pm$ 12 HV, which were higher than SLM 304L and most conventionally manufactured austenitic ODS alloys. The increase in YS of SLM 304L ODS alloy, compared to SLM 304L, was mainly attributed to the dispersion of nanoparticles, while the enhancement in ductility was caused by a higher rate of work hardening in larger grains due to the higher dislocation accumulation capacity of larger grains.

Declaration of competing interest

The authors declare that they have no known competing financial interests or personal relationships that could have appeared to influence the work reported in this paper.

CRediT authorship contribution statement

Milad Ghayoor: Data curation, Formal analysis, Writing - original draft. **Kijoon Lee:** Conceptualization, Validation. **Yujuan He:** Conceptualization, Validation. **Chih-hung Chang:** Funding acquisition, Project administration. **Brian K. Paul:** Funding acquisition, Project administration. **Somayeh Pasebani:** Supervision, Writing - original draft.

Acknowledgment

The authors would like to acknowledge the funding of critical equipment provided by the Murdock Charitable Trust (contract number: 2016231:MNL:5/18/2017), the RAPID Institute and U.S. DOE (contract number: DE-EE0007888) for the financial support. The authors also thank OSU electron microscopy center and ATAMI facility staff and director.

References

[1] N. Akasaka, S. Yamashita, T. Yoshitake, S. Ukai, A. Kimura, Microstructural changes of neutron irradiated ODS ferritic and martensitic steels, J. Nucl. Mater. 329 (2004) 1053–1056.
[2] K. Murty, I. Charit, Structural materials for Gen-IV nuclear reactors: challenges and opportunities, J. Nucl. Mater. 383 (1–2) (2008) 189–195.
[3] G.R. Odette, M.J. Alinger, B.D. Wirth, Recent developments in irradiation-resistant steels, Annu. Rev. Mater. Res. 38 (1) (2008) 471–503.
[4] H. Oka, M. Watanabe, S. Ohnuki, N. Hashimoto, S. Yamashita, S. Ohtsuka, Effects of milling process and alloying additions on oxide particle dispersion in austenitic stainless steel, J. Nucl. Mater. 447 (1–3) (2014) 248–253.
[5] Y. Miao, K. Mo, B. Cui, W.-Y. Chen, M.K. Miller, K.A. Powers, V. McCreary, D. Gross, J. Almer, I.M. Robertson, J.F. Stubbins, The interfacial orientation relationship of oxide nanoparticles in a hafnium-containing oxide dispersion-strengthened austenitic stainless steel, Mater. Char. 101 (2015) 136–143.
[6] M.A. Auger, V. De Castro, T. Leguey, A. Muñoz, R. Pareja, Microstructure and mechanical behavior of ODS and non-ODS Fe–14Cr model alloys produced by spark plasma sintering, J. Nucl. Mater. 436 (1–3) (2013) 68–75.
[7] X. Yan, X. Zhang, F. Wang, T. Stockdale, Y. Dzenis, M. Nastasi, B. Cui, Fabrication of ODS austenitic steels and CoCrFeNi high-entropy alloys by spark plasma sintering for nuclear energy applications, JOM 71 (8) (2019) 2856–2867.
[8] L. Raman, K. Gothandapani, B.S. Murty, Austenitic oxide dispersion strengthened steels : a review, Defence Sci. J. 66 (4) (2016) 316.
[9] D. Morrall, J. Gao, Z. Zhang, K. Yabuuchi, A. Kimura, T. Ishizaki, Y. Maruno, Tensile properties of mechanically alloyed Zr added austenitic stainless steel, Nuclear Materials and Energy 15 (2018) 92–96.
[10] Z. Zhou, S. Yang, W. Chen, L. Liao, Y. Xu, Processing and characterization of a hipped oxide dispersion strengthened austenitic steel, J. Nucl. Mater. 428 (1–3) (2012) 31–34.
[11] Y. Xu, Z. Zhou, M. Li, P. He, Fabrication and characterization of ODS austenitic steels, J. Nucl. Mater. 417 (1–3) (2011) 283–285.
[12] S. Pasebani, I. Charit, Y. Wu, J. Burns, K.N. Allahar, D.P. Butt, J.I. Cole, S. F. Alsagabi, Lanthana-bearing nanostructured ferritic steels via spark plasma sintering, J. Nucl. Mater. 470 (2016) 297–306.

[13] P. Koncz, Á. Horváth, K. Balázsi, F.Ç. Şahin, G. Göller, Y. Onüralp, C. Balázsi, Correlation between milling parameters, structural and mechanical properties of nanostructured austenitic Y_2O_3 strengthened steels, Mater. Sci. Forum 729 (2012) 409–414.
[14] S. Pasebani, A.K. Dutt, J. Burns, I. Charit, R.S. Mishra, Oxide dispersion strengthened nickel based alloys via spark plasma sintering, Mater. Sci. Eng., A 630 (2015) 155–169.
[15] T. Vanherck, G. Jean, M. Gonon, J. Lobry, F. Cambier, Spark plasma sintering: homogenization of the compact temperature field for non conductive materials, Int. J. Appl. Ceram. Technol. 12 (2015) E1–E12.
[16] J.R. Rieken, I.E. Anderson, M.J. Kramer, G. Odette, E. Stergar, E. Haney, Reactive gas atomization processing for Fe-based ODS alloys, J. Nucl. Mater. 428 (1–3) (2012) 65–75.
[17] C. Doñate-Buendía, F. Frömel, M.B. Wilms, R. Streubel, J. Tenkamp, T. Hupfeld, M. Nachev, E. Gökce, A. Weisheit, S. Barcikowski, F. Walther, J.H. Schleifenbaum, B. Gökce, Oxide dispersion-strengthened alloys generated by laser metal deposition of laser-generated nanoparticle-metal powder composites, Mater. Des. 154 (2018) 360–369.
[18] B. Mueller, Additive manufacturing technologies–Rapid prototyping to direct digital manufacturing, Assemb. Autom. 32 (2) (2012).
[19] B. Vayre, F. Vignat, F. Villeneuve, Metallic additive manufacturing: state-of-the-art review and prospects, Mechanics & Industry 13 (2) (2012) 89–96.
[20] S. Mirzababaei, S. Pasebani, A review on binder jet additive manufacturing of 316L stainless steel, Journal of Manufacturing and Materials Processing 3 (3) (2019) 82.
[21] W.E. Frazier, Metal additive manufacturing: a review, J. Mater. Eng. Perform. 23 (6) (2014) 1917–1928.
[22] X. Li, C. Kang, H. Huang, L. Zhang, T.B. Sercombe, Selective laser melting of an Al86Ni6Y4. 5Co2La1. 5 metallic glass: processing, microstructure evolution and mechanical properties, Mater. Sci. Eng., A 606 (2014) 370–379.
[23] M. Nematollahi, G. Toker, S. Saghaian, J. Salazar, M. Mahtabi, O. Benafan, H. Karaca, M. Elahinia, Additive manufacturing of Ni-rich NiTiHf 20: manufacturability, composition, density, and transformation behavior, Shape Memory and Superelasticity 5 (1) (2019) 113–124.
[24] S. Pasebani, M. Ghayoor, S. Badwe, H. Irrinki, S.V. Atre, Effects of atomizing media and post processing on mechanical properties of 17-4 PH stainless steel manufactured via selective laser melting, Additive Manufacturing 22 (2018) 127–137.
[25] M. Nematollahi, K.S. Baghbaderani, A. Amerinatanzi, H. Zamanian, M. Elahinia, Application of NiTi in assistive and rehabilitation devices: a review, Bioengineering 6 (2) (2019) 37.
[26] M. Ghayoor, S.B. Badwe, H. Irrinki, S.V. Atre, S. Pasebani, Water atomized 17-4 PH stainless steel powder as a cheaper alternative powder feedstock for selective laser melting, in: Materials Science Forum. 2018. Trans Tech Publ, vol. 941, 2018, pp. 698–703.
[27] R.M. Hunt, K.J. Kramer, B. El-Dasher, Selective laser sintering of MA956 oxide dispersion strengthened steel, J. Nucl. Mater. 464 (2015) 80–85.
[28] T. Boegelein, S.N. Dryepondt, A. Pandey, K. Dawson, G.J. Tatlock, Mechanical response and deformation mechanisms of ferritic oxide dispersion strengthened steel structures produced by selective laser melting, Acta Mater. 87 (2015) 201–215.
[29] J.C. Walker, K.M. Berggreen, A.R. Jones, C.J. Sutcliffe, Fabrication of Fe-Cr-Al oxide dispersion strengthened PM2000 alloy using selective laser melting, Adv. Eng. Mater. 11 (7) (2009) 541–546.
[30] J.N. DuPont, Fundamentals of Weld Solidification, ASM Handbook, 2011, p. 6A.
[31] N.B. Dahotre, S. Harimkar, Laser Fabrication and Machining of Materials, Springer Science & Business Media, 2008.
[32] M. Ghayoor, K. Lee, Y. He, C.h. Chang, B.K. Paul, S. Pasebani, Selective laser melting of 304L stainless steel: role of volumetric energy density on the microstructure, texture and mechanical properties, Additive Manufacturing 32 (2020) 101011.
[33] M. Wang, Z. Zhou, H. Sun, H. Hu, S. Li, Microstructural observation and tensile properties of ODS-304 austenitic steel, Mater. Sci. Eng., A 559 (2013) 287–292.
[34] Z. Wang, J. Wang, G. Yang, Phase field investigation on cellular tip splitting during directional solidification, Scripta Mater. 61 (9) (2009) 915–918.
[35] B. AlMangour, D. Grzesiak, T. Borkar, J.-M. Yang, Densification behavior, microstructural evolution, and mechanical properties of TiC/316L stainless steel nanocomposites fabricated by selective laser melting, Mater. Des. 138 (2018) 119–128.
[36] B. AlMangour, M.-S. Baek, D. Grzesiak, K.-A. Lee, Strengthening of stainless steel by titanium carbide addition and grain refinement during selective laser melting, Mater. Sci. Eng., A 712 (2018) 812–818.
[37] M. Ghayoor, S. Mirzababaei, K. Lee, Y. He, C.-h. Chang, B.K. Paul, S. Pasebani, Strengthening of 304L stainless steel by addition of yttrium oxide and grain refinement during selective laser melting, in: Proceedings of the 30th Annual International Solid Freeform Fabrication Symposium – an Additive Manufacturing Conference. 2019, 2019, pp. 967–976. Austin, TX.
[38] K. Verhiest, S. Mullens, J. Paul, I. De Graeve, N. De Wispelaere, S. Claessens, A. DeBremaecker, K. Verbeken, Experimental study on the contact angle formation of solidified iron–chromium droplets onto yttria ceramic substrates for the yttria/ferrous alloy system with variable chromium content, Ceram. Int. 40 (1) (2014) 2187–2200.
[39] N. Cunningham, Y. Wu, D. Klingensmith, G.R. Odette, On the remarkable thermal stability of nanostructured ferritic alloys, Mater. Sci. Eng., A 613 (2014) 296–305.
[40] H. Xu, Z. Lu, S. Ukai, N. Oono, C. Liu, Effects of annealing temperature on nanoscale particles in oxide dispersion strengthened Fe-15Cr alloy powders with Ti and Zr additions, J. Alloys Compd. 693 (2017) 177–187.
[41] M. Wang, Z. Zhou, H. Sun, H. Hu, S. Li, Effects of plastic deformations on microstructure and mechanical properties of ODS-310 austenitic steel, J. Nucl. Mater. 430 (1–3) (2012) 259–263.
[42] A. Standard, Standard Specification for Chromium and Chromium-Nickel Stainless Steel Plate, Sheet, and Strip for Pressure Vessels and for General Applications. 2017, ASTM, West Conshohocken, PA, 2017.
[43] T.-K. Kim, C.-S. Bae, D.-H. Kim, J.-S. Jang, S.-H. Kim, C.-B. Lee, D.-H. Hahn, Microstructural observation and tensile isotropy of an austenitic ODS steel, Nuclear Engineering and Technology 40 (4) (2008) 305–310.
[44] D. Gu, W. Meiners, K. Wissenbach, R. Poprawe, Laser additive manufacturing of metallic components: materials, processes and mechanisms, Int. Mater. Rev. 57 (3) (2012) 133–164.
[45] B. AlMangour, D. Grzesiak, J.-M. Yang, Rapid fabrication of bulk-form TiB_2/316L stainless steel nanocomposites with novel reinforcement architecture and improved performance by selective laser melting, J. Alloys Compd. 680 (2016) 480–493.
[46] X.P. Li, G. Ji, Z. Chen, A. Addad, Y. Wu, H. Wang, J. Vleugels, J. Van Humbeeck, J.-P. Kruth, Selective laser melting of nano-TiB2 decorated AlSi10Mg alloy with high fracture strength and ductility, Acta Mater. 129 (2017) 183–193.
[47] V. Mudavakkat, V. Atuchin, V. Kruchinin, A. Kayani, C. Ramana, Structure, morphology and optical properties of nanocrystalline yttrium oxide (Y_2O_3) thin films, Opt. Mater. 34 (5) (2012) 893–900.
[48] C. Boley, S.A. Khairallah, A.M. Rubenchik, Calculation of laser absorption by metal powders in additive manufacturing, Applied optics 54 (9) (2015) 2477–2482.
[49] D. Gu, G. Meng, C. Li, W. Meiners, R. Poprawe, Selective laser melting of TiC/Ti bulk nanocomposites: influence of nanoscale reinforcement, Scripta Mater. 67 (2) (2012) 185–188.
[50] A. Simchi, H. Pohl, Effects of laser sintering processing parameters on the microstructure and densification of iron powder, Mater. Sci. Eng. 359 (1–2) (2003) 119–128.
[51] D. Stefanescu, B. Dhindaw, S. Kacar, A. Moitra, Behavior of ceramic particles at the solid-liquid metal interface in metal matrix composites, Metallurgical Transactions A 19 (11) (1988) 2847–2855.
[52] U.S. Bertoli, G. Guss, S. Wu, M.J. Matthews, J.M. Schoenung, In-situ characterization of laser-powder interaction and cooling rates through high-speed imaging of powder bed fusion additive manufacturing, Mater. Des. 135 (2017) 385–396.
[53] L.J. Alvarez, M.A. San Miguel, J.A. Odriozola, Effects of nonstoichiometry in the melting process of Y 2 O 3 from molecular dynamics simulations, Phys. Rev. B 59 (17) (1999) 11303.
[54] H. Okamoto, OY (Oxygen-Yttrium), J. Phase Equilibria Diffus. 32 (6) (2011), 574-574.
[55] Y. Li, K. Zhou, P. Tan, S.B. Tor, C.K. Chua, K.F. Leong, Modeling temperature and residual stress fields in selective laser melting, Int. J. Mech. Sci. 136 (2018) 24–35.
[56] J. Nelson, D. Riley, An experimental investigation of extrapolation methods in the dimensions of crystals derivation of accurate unit-cell, in: Proc. Phys. Soc. (London), vol. 57, 1945, pp. 160–177, 1945.
[57] J. Chambers, G. Parsons, Physical and electrical characterization of ultrathin yttrium silicate insulators on silicon, J. Appl. Phys. 90 (2) (2001) 918–933.
[58] L.-Y. Chen, J.-Q. Xu, H. Choi, M. Pozuelo, X. Ma, S. Bhowmick, J.-M. Yang, S. Mathaudhu, X.-C. Li, Processing and properties of magnesium containing a dense uniform dispersion of nanoparticles, Nature 528 (7583) (2015) 539.
[59] S. Rajasekhara, P. Ferreira, L. Karjalainen, A. Kyröläinen, Hall–Petch behavior in ultra-fine-grained AISI 301LN stainless steel, Metall. Mater. Trans. 38 (6) (2007) 1202–1210.
[60] J. Bailey, P. Hirsch, The dislocation distribution, flow stress, and stored energy in cold-worked polycrystalline silver, Phil. Mag. 5 (53) (1960) 485–497.
[61] J.G. Sevillano, I.O. Arizcorreta, L. Kubin, Intrinsic size effects in plasticity by dislocation glide, Mater. Sci. Eng., A 309 (2001) 393–405.
[62] T. Gladman, D. Dulieu, I. McIvor, Microalloying 75, Union Carbide Corp, New York (NY), 1977, p. 32.
[63] N. Hansen, Hall–Petch relation and boundary strengthening, Scripta Mater. 51 (8) (2004) 801–806.
[64] H. Wan, Z. Zhou, C. Li, G. Chen, G. Zhang, Effect of scanning strategy on mechanical properties of selective laser melted Inconel 718, Mater. Sci. Eng., A 753 (2019) 42–48.
[65] M. Alinger, G. Odette, D. Hoelzer, On the role of alloy composition and processing parameters in nanocluster formation and dispersion strengthening in nanostuctured ferritic alloys, Acta Mater. 57 (2) (2009) 392–406.
[66] S. Pasebani, P. Samimi, M. Saber, Effects of scandium and hafnium solute additions on microstructure thermal stability in nanostructured ferritic alloys, Mater. Char. 151 (2019) 216–220.
[67] L. Ratke, P.W. Voorhees, Growth and Coarsening: Ostwald Ripening in Material Processing, Springer Science & Business Media, 2013.
[68] Y. Zhao, Y. Zhu, E.J. Lavernia, Strategies for improving tensile ductility of bulk nanostructured materials, Adv. Eng. Mater. 12 (8) (2010) 769–778.
[69] I. Sabirov, M.Y. Murashkin, R. Valiev, Nanostructured aluminium alloys produced by severe plastic deformation: new horizons in development, Mater. Sci. Eng. 560 (2013) 1–24.
[70] E. Ma, Eight routes to improve the tensile ductility of bulk nanostructured metals and alloys, JOM 58 (4) (2006) 49–53.
[71] Y. Wang, M. Chen, F. Zhou, E. Ma, High tensile ductility in a nanostructured metal, Nature 419 (6910) (2002) 912.